Loss-reduction in midinfrared photonic crystal quantum cascade lasers using metallic waveguides

Gangyi Xu
Raffaele Colombelli
Institut d'Electronique Fondamentale
Université Paris-Sud
UMR8622 CNRS
91405 Orsay, France
E-mail: raffaele.colombelli@u-psud.fr

Gregoire Beaudoin
Ludovic Largeau
Olivia Mauguin
Isabelle Sagnes
Laboratoire de Photonique et Nanostructures
LPN/CNRS
Route de Nozay
91460 Marcoussis, France

Abstract. We describe a mechanism for plasmonic loss reduction in midinfrared metallic photonic crystals and apply it to surface-plasmon quantum cascade lasers. We obtain pulsed, room-temperature operation of surface-emitting photonic crystal quantum cascade lasers operating at $\lambda \approx 7.4$ μm. The photonic crystal resonator is patterned in the device top metallization, and laser operation is obtained on a band-edge mode of the photonic band structure. The emission is spectrally single mode, with a side-mode suppression ratio of 20 dB, and on-chip tunability is obtained over a wavelength range of ≈ 0.52 μm. Simulations based on a finite elements approach and on the finite-difference time-domain method allow us to study the photonic-band structure, the electromagnetic field distributions, and especially, the influence of the device parameters on the losses. The comparison between the measured and simulated far-field emission patterns and polarization proves the lasers operate on a monopolar-symmetry mode © *2010 Society of Photo-Optical Instrumentation Engineers.* [DOI: 10.1117/1.3516518]

1 Introduction

The combination of photonic-crystal (PhC) technology and quantum cascade (QC) lasers has attracted recent interest for their significant advantages in tailoring and engineering the spectral and spatial characteristics of the devices.[1–11] To date, PhC QC lasers have been demonstrated both in the midinfrared (mid-IR) and terahertz spectral ranges. When surface emission is important, the so-called *band-edge* configuration is preferred, with the device operating on band-edge, low-group-velocity states of the photonic band structure. These states, typically located at high-symmetry points in the band structure, exhibit a high photonic density of states as a result of the two-dimensional distributed feedback of the photonic lattice.

PhC QC lasers have been implemented in a large variety of geometries, schemes, and structures. A main classification into two different families, which are strong and weak-index-contrast PhC structures, can be proposed. In the former case, the index contrast is comparable to the value of the material with high refractive index in the PhC structure.[1–7] For III-V semiconductors, this value is typically 3/3.5. Strong optical feedback can be achieved, which is crucial to implement compact PhC QC lasers, or even microcavity devices, which operate on a defect mode of the PhC structure. In the latter case instead, the index contrast achievable is much lower than the indices of refraction of the semiconductor materials.[8,9] A much larger number of PhC periods is needed to achieve sufficient optical feedback for laser action. The large area of these PhC structures, and especially the delocalization of the electromagnetic (EM) field across the whole device surface, makes them appealing for highly directional surface-emitting QC lasers with reasonably high output power.

Examples of mid-IR high-index-contrast PhC structures can be found in Refs. 1 and 7, where airholes deeply etched into the semiconductor material lead to strong index contrast (3.4 versus 1). In the case of Ref. 1, a functional, surface-emitting laser needs only 10 PhC periods from the center. When a metal-metal waveguide can be employed, as in THz QC lasers,[12] a deep semiconductor etch is not even necessary,[4] and the PhC can be directly printed in the top metallization. Thanks to the extremely subwavelength thickness of the structure, a large index contrast is still obtained (approximately 3.6 versus 2.8).

Recently, we demonstrated a surface-emitting QC laser that employs a low-index-contrast PhC resonator[8] and operates in the mid-IR range of the EM spectrum. A surface-plasmon waveguide is used, with a PhC pattern directly "*written*" onto the device top metallization, which acts also as contact for current injection. Although the geometry is similar to the THz PhC QC lasers of Refs. 4–6, the underlying physical mechanism is significantly different. In the mid-IR structure[8], the waveguide thickness (which includes the active region and the substrate) is one order of magnitude larger than the wavelength. Because the penetration of the EM field inside the semiconductor is only marginally affected by the presence/absence of the top metallization, a very weak *effective* index contrast (about 3.2 versus 3.1, estimated with a 1-D transfer-matrix calculation) can be obtained. However, the metallic PhC strongly modulates the mode profile. In the regions with top metallization, a surface-plasmon is present, the electric field is bound to the top metal-semiconductor interface and decays approximately exponentially into the active region. In the regions *without* metallization (i.e., in the airholes), the electric field is instead maximum at the center of the active layer, it decays toward the air-claddings and substrate, respectively, and its intensity is minimum at the top air-semiconductor interface. This modal mismatch leads

to an *effective* index contrast and eventually yields the optical feedback necessary for laser action.

In our first results, we have demonstrated single-mode surface emission with reduced output divergence.[8] The spatial character of the laser emission (the far-field pattern and polarization), could be precisely controlled by engineering the shape, symmetry, and phase of the PhC structure.[9] However, the maximum operating temperature (T_{max}) was limited to 240 K in those devices.

In this paper, we report the pulsed, room-temperature operation of mid-IR surface-emitting QC lasers with metallic PhC. We demonstrate that a mechanism for reducing the plasmonic losses *via* metal patterning can be successfully implemented in 2-D systems. Metallic PhC structures have been already proposed as optical resonators for QC lasers,[4,13] however, the mechanism of mode selection and loss reduction is still unclear. In this work, we implement 3-D finite-difference time-domain (FDTD) simulations to analyze the mode distribution and the device losses. In particular, the complex refractive index of *both* metal and semiconductors are taken into account, which allows us to simultaneously deduce each component of the loss, including the material loss and the cavity loss. This accurate analysis has played a crucial role to modify the PhC structure and reduce the threshold. In Ref. 14, we had identified a configuration of the top metal that sustains new modes with extremely low propagation losses with respect to standard SPs. In this paper, we show that the Bloch states with monopolar symmetry in metallic photonic crystals can exhibit a similar property.

The paper is organized as follows. In Section 2 the design of the PhC QC laser is described: the photonic band structure and mode distributions are analyzed, the device losses are determined, and an optimized PhC cavity is proposed. Section 3 details the material growth and the device fabrication. Section 4 reports the experimental results: Spectral and spatial laser characterizations, as well as the temperature behavior. The lasing mode identification is obtained by comparing the measured far-field patterns and polarization with FDTD simulations. Conclusions are drawn in Section 6.

2 Design

Figure 1(a) shows the schematic structure of a typical PhC QC laser studied in this work. A metallic PhC, which features a triangular lattice of airholes in a thin Ti/Au film (3/80 nm), is directly "written" on top of the active region. The Ti/Au pattern serves simultaneously as contact for current injection and as surface plasmon carrying layer. In the region under the Ti/Au pattern, the electric field is bound at the metal/semiconductor interface and decays approximately exponentially into the active region. Below the airholes, in the z direction, the electric field is confined near the center of the active region and decays toward the airinterface and the substrate, respectively. This modal mismatch of the field profiles is responsible for optical feedback.

The photonic band structure [Fig. 1(b)] is numerically calculated—within a finite element approach, The finite elements solver "Comsol Multiphysics" has been employed for the simulations by simulating the 3-D unit cell with Bloch periodic boundary conditions. Figure 1(b) reports a close-up of the photonic band structure near the Γ point. The six band-edge states are of special interest: their flat dispersion yields an enhanced photonic density of states, which makes them
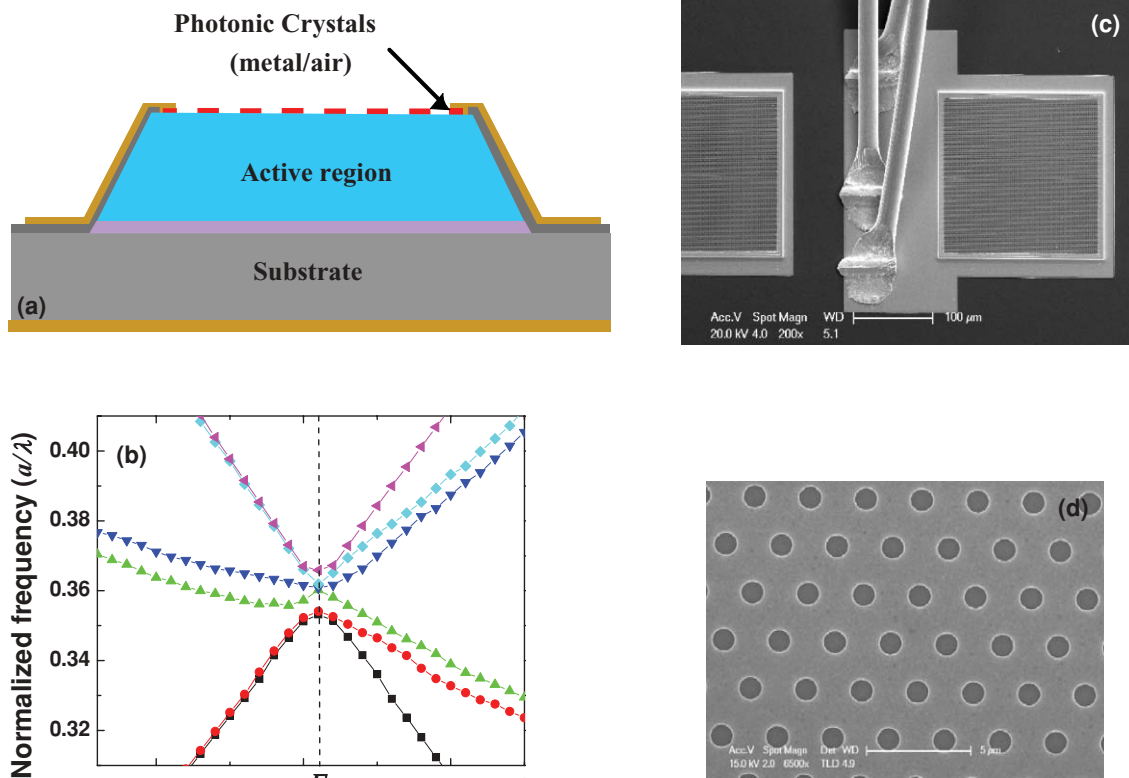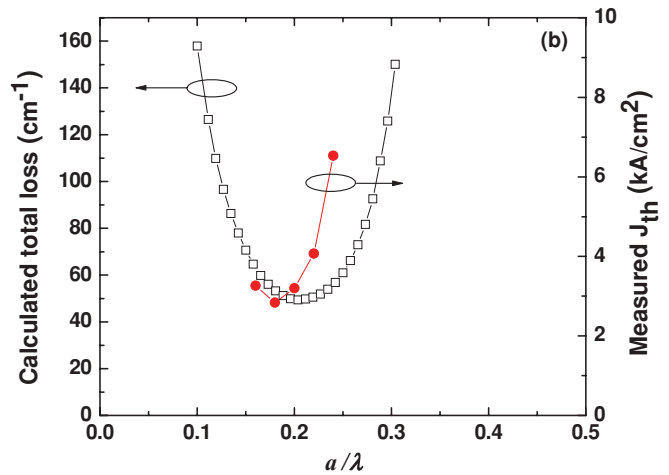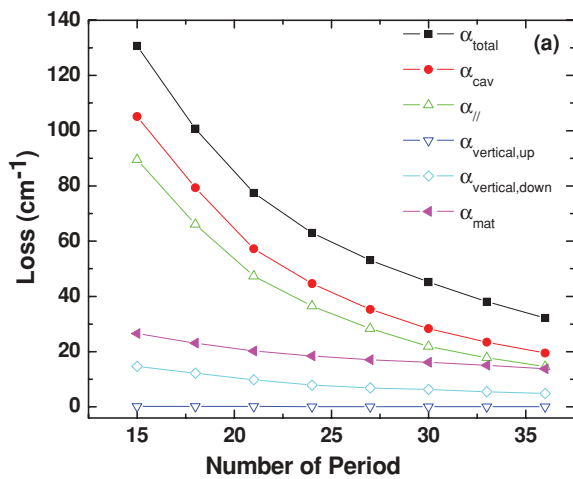

Fig. 1 (a) Schematic cross section of a PhC device, (b) calculated photonic band structure of the PhC structure employed in this work, (c) SEM image of a typical device, and (d) close-up of the metallic photonic crystal structure that is directly "written" on the top device metallization.
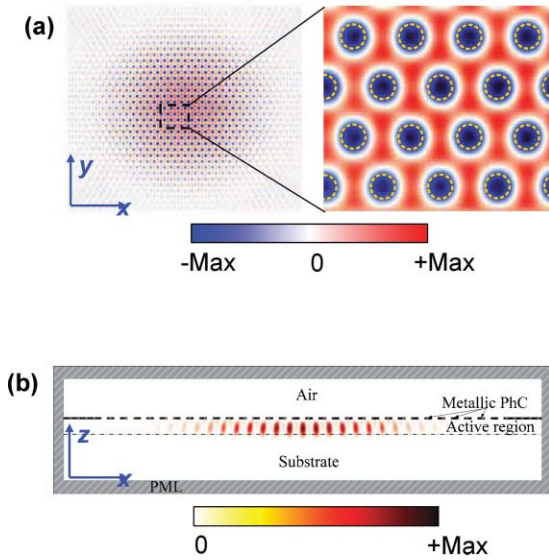
Fig. 2 (a) Electric field distribution (E_z component, orthogonal to the semiconductor layers) of the monopole mode. An *x-y* section has been taken at the center of the laser active region. (b) Light intensity {$[E(\omega)^* D(\omega) + H(\omega)^* B(\omega)]/2$} distribution for monopole mode in an *x-z* section across the PhC center. The simulation domain is also shown.

good candidates for lasing. Furthermore, surface emission will be achieved because the modes are located *above* the light cone. Ultimately, the band-edge mode with lowest *total losses* will be lasing. The total losses include two contributions: the material (α_{mat}) and the cavity (α_{cav}) loss. The latter one can be further divided into in-plane ($\alpha_{//}$) loss, the radiation loss coupled to the free space ($\alpha_{vertical, up}$), and coupled to the substrate ($\alpha_{vertical, down}$), respectively.

We first estimate the material loss by simulating an infinite structure, within a 3-D finite elements approach, with Bloch periodic boundary conditions. The calculations yield $\alpha_{mat} = 11$ cm^{-1} for the highest frequency mode

($a/\lambda = 0.366$). This value is significantly lower than for the other band-edge modes, whose losses are higher than 30 cm^{-1}. Here, *a* is the lattice period of the PhC, and λ is the free-space wavelength. The electric field distribution of this mode has monopolar symmetry, and its loss is also significantly lower than for a standard surface plasmon mode (45 cm^{-1}) in a uniformly metalized device, thus suggesting that a 2-D metallic pattern can sustain low-loss modes.

The finite size of the photonic crystal has a crucial effect on the device loss and mode distribution. We therefore implemented 3-D FDTD simulations,[7,15,16] where the complex refractive index of the materials are used. It allows us to deduce, simultaneously, the material loss and each component of the cavity loss. The numerical calculations show that, for a finite PhC structure, only the monopole mode exhibits a stable mode distribution. It strongly suggests that only the monopole mode has a sufficiently low total loss. Figure 2(a) presents the distribution of the *z* component of the electric field (E_z) for the monopole mode. The section is taken parallel to the *x-y* plane and in the center of the active region. Figure 2(b) shows instead the energy distribution in the *x-z* section across the center of the PhC. The EM field is confined in the active region *and* under the airholes, with a weak overlap with the metallic pattern. This characteristic explains why α_{mat} for the monopole mode is much lower than for a standard SP mode. Note that this mechanism of loss reduction is different from the one reported in Ref. 2, where the effect originates from the presence of an in-plane electric field in regions with lower index of refraction, and also from better thermal management.

Monopolar Bloch modes of infinite PhC structures do not couple with the *continuum* of radiative modes, because the relative surface transverse fields are antisymmetric.[17,18] In fact, surface emission is instead a consequence of the *finite* size of the devices. We calculated the influence of the PhC parameters, including the normalized radius (*r/a*) of the airhole and the number of periods (*N*), on the loss of the monopole mode. Figure 3(a) shows the calculated total loss and its constituent components as a function of *N*, where *r/a*

Fig. 3 (a) The total loss and its constituent components as a function of *N*, calculated by 3-D FDTD simulation. *r/a* is fixed at 0.2; α_{total} is the total loss, α_{cav} the cavity loss, and α_{mat} the material loss, $\alpha_{//}$ the in-plane cavity loss, and $\alpha_{vertical,up}$ and $\alpha_{vertical,down}$ are the radiation loss coupled to free space and the substrate, respectively. The complex refractive index used for metal, active region, and substrate are $n_{metal} = 4.2 + 53.2 \cdot i$, $n_{AR} = 3.27 + 6.72 \times 10^{-5} \cdot i$, and $n_{sub} = 2.85 + 5.86 \times 10^{-3} \cdot i$, respectively. (b) The calculated total loss and the measured laser threshold as a function of *r/a*. The values of *a* and *N* are 2.70 μm and 28, respectively. The threshold was measured at 78 K in pulsed mode (50-ns pulse width at an 84-kHz repetition rate).

is fixed at its optimized value. Figure. 3(a) shows that the total loss is mainly caused by the in-plane cavity loss ($\alpha_{//}$) and material loss (α_{mat}), and it decreases gradually by increasing N. For the PhC with small N ($N = 15$) $\alpha_{//}$ is the dominant effect that limits the device threshold. $\alpha_{//}$ decrease rapidly by increasing N and become comparable to α_{mat} for the PhC with large N ($N = 36$). On the other hand, α_{mat} decreases slowly when N increases, caused by the nonperiodic distribution of the EM fields in a finite PhC structure. We note the good convergence between Final element Method the (FEM) and the FDTD simulations. For instance, the α_{mat} for a large PhC structure ($N = 36$) calculated by FDTD equals to 13 cm^{-1}, where as the α_{mat} for an infinite PhC calculated by FEM is 11 cm^{-1}. In addition, the radiation loss coupled to the free space ($\alpha_{vertical, up}$) is in the order of 0.1 cm^{-1}. Such a low radiation loss originates from the antisymmetric distributions of the relative surface transverse fields and indicates low extraction efficiency. In order to reach a sufficiently low total loss— and, hence, a reduced current threshold—a large number of PhC periods is necessary.

Figure 3(b) presents the influence of the r/a on the total loss, where the value of N is fixed as 28. Figure 3(b) indicates that the device loss is sensitive to the radius of airholes. The total loss reaches a minimum for $r/a \approx 0.2$ and increases rapidly when r/a deviates from this optimal value.

3 Material Growth and Device Process

The laser structure (sample E-InP281) was grown by metalorganic vapor-phase epitaxy, in the In$_{0.53}$Ga$_{0.47}$As/Al$_{0.48}$In$_{0.52}$As material system lattice matched to a highly doped InP substrate. The details of the growth are given in Ref. 19. The active region is based on a two-phonon-resonance design with the nominal lasing transition at $\lambda = 7.5$ μm. Fifty active-region/injector stages were grown, preceded by a 2-μm-thick low-doped InP ($n = 1 \times 10^{17}$ cm^{-3}) buffer layer and a 500-nm-thick InGaAs cladding ($n = 5 \times 10^{16}$ cm^{-3}), and followed by doped, InGaAs contact facilitating layers.

The device process started by defining the PhC pattern by e-beam lithography, using a two-layer resist mask (PMMA and FOx12),[20] followed by metal evaporation (Ti/Au, 3/80 nm) and liftoff. A series of PhC patterns with different lattice periods (a), radius of airhole (r), and N are tested. After defining the top metallic contact size and shape by wet chemical etching, mesa cavities were wet etched down to the InP substrate, for current confinement purposes. The sidewall of the cavity and the edge of top mesa were covered by 200-nm-thick Si$_x$N$_y$ for electrical insulation. The top electrode was formed by evaporating a Ti/Au layer that surrounded and contacted the edge of the PC pattern. Substrate thinning down to 250 μm, polishing, and back contact deposition concluded the processing. The devices have then been mounted with indium solder on copper blocks, wire bonded, and loaded on a temperature-controlled cold finger of a liquid-nitrogen continuous flow cryostat for device characterization. Figures 1(c) and 1(d) show scanning electron microscopy (SEM) images of a typical device, and a close-up of the metallic PhC structure, respectively.

4 Experimental Results and Discussions

Figure 4 shows the lasing spectra of several devices with the same value of $r/a = 0.2$, but different lattice periods. The spectra were measured at a temperature of 78 K in
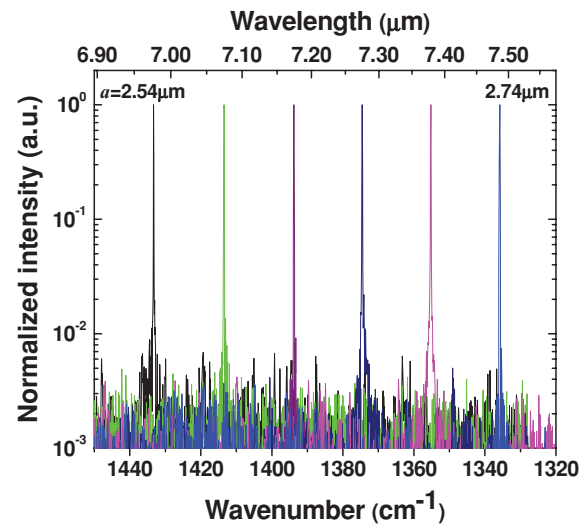
**Fig. 4** Lasing spectra of several devices with the same $r/a = 0.2$ and with different lattice periods a (from 2.54 to 2.74 μm, in steps of 40 nm). The spectra were acquired at a heat-sink temperature of 78 K, using a Nicolet FTIR spectrometer, equipped with a liquid-nitrogen-cooled HgCdTe detector. The lasers were operated in pulsed mode, with a repetition rate of 84 kHz and pulse widths of 20 ns.

pulsed mode. Single-mode emission with a side-mode suppression ratio (SMSR) of at least ≈ 20 dB was observed for all the devices. The emission wavelength tunes linearly with the lattice period, corresponding to a normalized frequency value $a/\lambda = 0.365$, in good agreement with the calculated frequency of the monopole mode. By lithographically tuning the lattice period a in the 2.54–2.74 μm range, the emission wavelength can be varied across a wide range of ~ 0.52 μm. For all the injected currents, operation temperatures, and photonic lattice periods explored, the devices operate in single mode. This feature demonstrates the robustness of the 2-D distributed feedback, and the large difference of loss between the lasing mode and the other band-edge modes, which evidently prevents mode competition effects.

For the photonic crystal quantum cascade lasers, the shape of the cavity and the boundary conditions has important effects on the mode distribution.[1,4,13] We have tested different cavity shapes, including irregular cavities, hexagonal cavities,[8] as well as the square cavity used in this work. In spite of the different cavity shapes, the devices always operate on the monopole mode. We attribute it to the special configuration of the cavity boundary. The photonic crystal cavity exhibits sloped sidewalls, thanks to the wet etching of the semiconductor mesa, and it is also covered by the Si$_x$N$_y$ passivating layer and Ti/Au metallization. Therefore, the EM field reaching the cavity boundary will be either absorbed or reflected into the highly doped substrate. As a result, an equivalent absorbing boundary condition is created and the EM field in the cavity will not be perturbed.

The influence of the PhC parameters (r/a and N) have also been investigated. With the fixed a ($= 2.70$ μm) and N ($= 28$), a series of lasers with different hole radius ($r/a = 0.1, 0.16, 0.18, 0.20, 0.22, 0.24, 0.30,$ and 0.40) have been fabricated. The threshold current densities (J_{th}) for these devices are measured at 78 K in pulsed mode, and the results are shown in Fig. 3(b). The measurements show
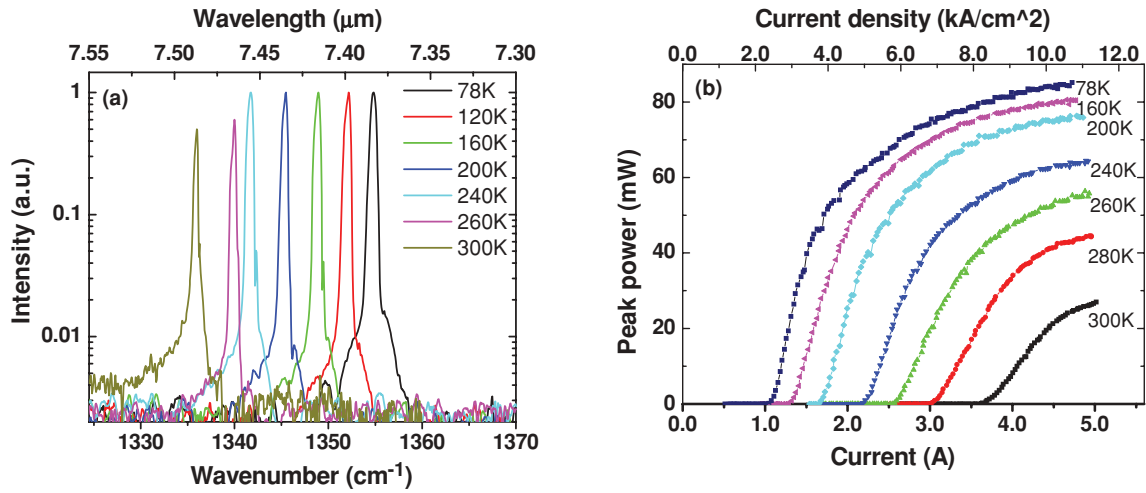
Fig. 5 (a) Laser spectra and (b) light-current curves measured at different temperatures for a device with optimized PhC parameters. The lattice period is $a = 2.70$ μm, $r/a = 0.20$, and $N = 38$. The lasers were measured in pulsed mode (50 ns pulse width at 84 kHz repetition rate).

that J_{th} reaches a minimum value when r/a equals 0.18, which is very close to the theoretically optimized value of r/a (0.20). The measured J_{th} increases rapidly when r/a deviates from the optimum value. For devices in which $r/a \leq 0.1$ or $r/a \geq 0.3$, neither lasing nor even resonances in the electroluminescence spectra can be observed. We have then characterized the influence of N on the laser performance, while keeping r/a at 0.20 (near the optimized value), and the lattice period at $a = 2.70$ μm. The J_{th} at 78 K decreases from 3.1 to 2.3 kA/cm^2 when N increases from 28 to 38. The T_{max} of the former device is 240 K, while the latter laser operates up to room temperature. The measurement results corroborate the reliability of the FDTD simulation.

Figure 5(a) shows the lasing spectra of a PhC device ($a = 2.70$ μm, $r/a = 0.20$, $N = 38$). The emission wavelength tunes linearly with the heat-sink temperature from $\lambda = 7.39$ μm at 78 K to $\lambda = 7.49$ μm at 300 K. The tuning rate is ≈ 0.45 nm/K. Figure 5(b) shows the L-I-V curves of the device at different temperatures. The threshold current density increases from 2.3 kA/cm^2 at 78 K to 8.2 kA/cm^2 at 300 K, while the peak output power decreases from 85 to 26 mW. For comparison, we have also fabricated the standard ridge QC lasers from the same epitaxial material and with uncoated facets. The ridge width and cavity length

are 20 μm and 1.5 mm, respectively. This corresponds to an emitting volume comparable to the PhC cavity. For the surface plasmon Fabry–Perot QC lasers, the J_{th} at 77 K is 2.5 kA/cm^2, and the T_{max} is 260 K, with only a few megawatts peak output power. The comparison demonstrates that by using metallic PhC patterning, the threshold and output power can be significantly improved.

We have measured the far-field pattern and the polarization characteristics of the lasers, because the comparison to the FDTD simulations allows the identification of the lasing mode. The results for a typical device are reported in Fig. 6(a). The $\theta_x = \theta_y = 0$ angle corresponds to the direction perfectly orthogonal to the device surface. The emission patterns have a "doughnut" shape, which is a characteristic feature of all PhC lasers operating on band-edge modes at the Γ-point of the photonic band structure.[21] The emission angular divergence is ≈ 9 deg. Figures 6(b) and 6(c) report two polarized far-field patterns, obtained by mounting a metallic grating polarizer in front of the LN$_2$-cooled HgCdTe detector (the polarization direction is indicated by the gray arrows). The polarized far-field exhibits two symmetric lobes along the polarization axis, while no emission is detected orthogonal to it. The experimental results suggest that the far-field is *radially* polarized.
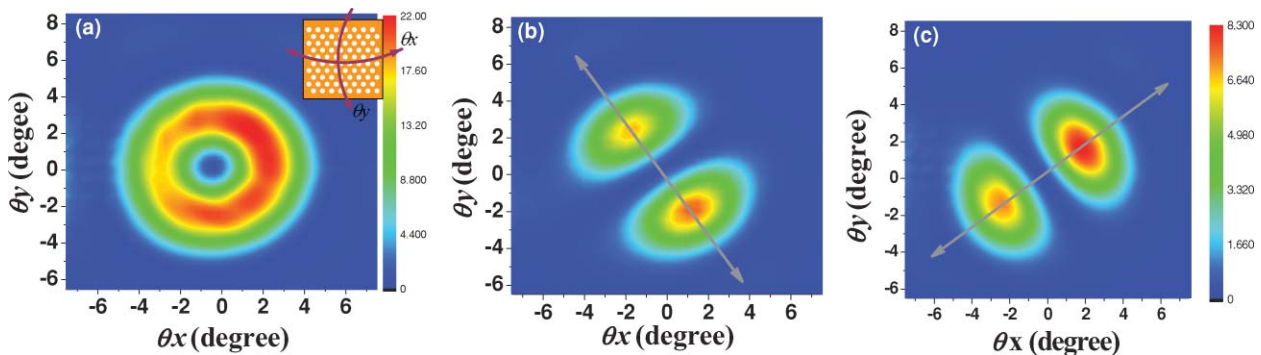
Fig. 6 (a) Far-field measured at 78 K in pulsed mode (50-ns pulse width at 84-kHz repetition rate). A liquid-nitrogen-cooled HgCdTe detector has been scanned on a 15-cm-radius sphere centered on the device surface. (b, c) Far-field patterns measured with a linear polarizer placed and fixed in front of the detector. The arrows indicate the polarization direction, and the inset of (a) defines the scan directions. The angular resolution is 0.5 deg.
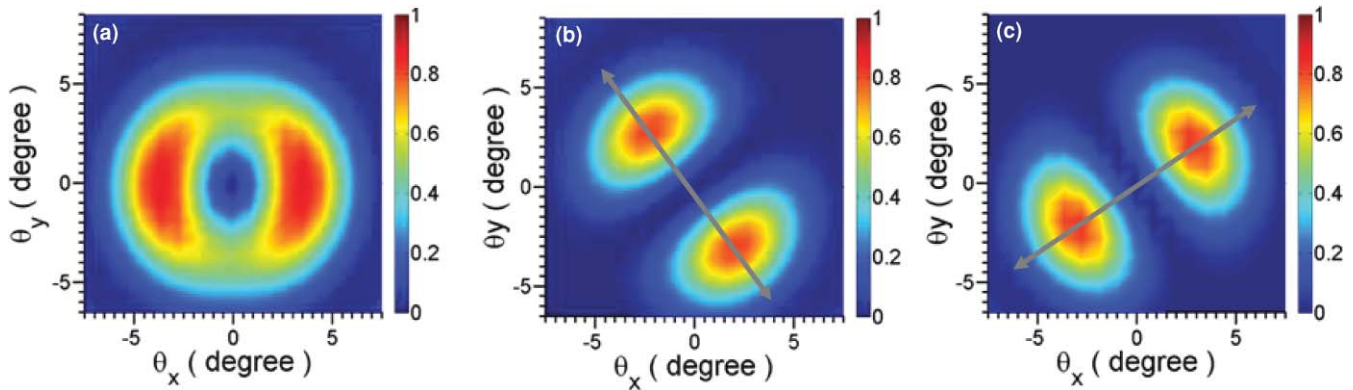
Fig. 7 Numerically simulated far-field pattern obtained using a 2-D FDTD approach: (a) Unpolarized far-field pattern, and (b), and (c) components of the far-field pattern polarized in the directions marked by the arrows. The symmetry and polarization are in excellent agreement with the experimental results in Fig. 6.

The numerically simulated far fields are reported in Fig. 7 (details of the simulation procedure can be found in Refs. 6, 9, 22, and 23. Figure 7(a) shows the calculated time-averaged intensity of the electric field ($|E|^2$) in the far field, whereas Figs. 7(b) and 7(c) report, instead, the calculated intensity of the *polarized* electric field. The gray arrows indicate the direction of the polarization and correspond to polarization direction used in the experiment [Figs. 6(b) and 6(c)]. The measured far-field patterns are in very good qualitative and *quantitative* agreement with the calculations. For instance, the calculated divergence angle of the far-field pattern is 11 deg, whrreas the measured one is 9 deg. This excellent agreement is conclusive evidence that the device operates on the monopolar Bloch mode.

5 Conclusions

We have systematically studied the emission properties of surface-plasmon PhC QC lasers in the mid-IR range. The photonic-band structure, the EM field distribution, and the loss of the band-edge modes are analyzed by means of FEM and FDTD numerical simulations. The influence of several PhC parameters is also calculated. The results indicate that only the monopole mode has a low-enough loss to support laser oscillations.

Spectrally single-mode surface emission is obtained, with a SMSR of ≈ 20 dB, and the emission wavelength is lithographically tunable across a 0.52 μm. Analysis of the far-field pattern and polarization, which has a divergence of only 9 deg, demonstrates that the lasing mode has monopolar symmetry.

Most importantly, by using optimized PhC parameters, pulsed room-temperature operation is achieved. The laser performances are obviously better than standard surface plasmon Fabry–Perot lasers fabricated from the same wafer. This finding indicates that the metal-patterning operates as a plasmonic loss-reduction mechanism also in 2-D (and not only in 1-D as in Ref. 14), and it opens up possible prospects of using PhCs as a performance-improvement tool. Further improvements of the PhC laser performance, in terms of threshold and output power, may come from modified photonic crystal designs and fabrication technologies. Dielectric waveguide combined with a shallow dry-etched photonic crystal structure can be employed. This strategy can lead to simultaneously decreased material and in-plane cavity losses

and, therefore, to room-temperature pulsed operation with very low threshold current density. In order to realize room-temperature continuous wave operation, an improved thermal dissipation approach, suitable to surface-emtting lasers, must be developed.

References

1. R. Colombelli, K. Srinivasan, M. Troccoli, O. Painter, C. Gmachl, D. M. Tennant, A. Sergent, D. L. Sivco, A. Y. Cho, and F. Capasso, *Science* **302**, 1374–1377 (2003).
2. H. Zhang, L. A. Dunbar, G. Scalari, R. Houdre, and J. Faist, *Opt. Express* **15**, 16818–16827 (2007).
3. A. Benz, Ch. Deutsch, G. Fasching, K. Unterrainer, A. M. Andrews, P. Klang, W. Schrenk, and G. Strasser, *Opt. Express* **17**, 941–946 (2009).
4. Y. Chassagneux, R. Colombelli, W. Maineult, S. Barbieri, H. Beere, D. Ritchie, S. P. Khanna, E. H. Linfield, and A. G. Davies, *Nature (London)* **457**, 174–178 (2009).
5. Y. Chassagneux, R. Colombelli, W. Maineult, S. Barbieri, S. P. Khanna, E. H. Linfield, and A. G. Davies, *Appl. Phys. Lett.* **96**, 031104 (2010).
6. Y. Chassagneux, R. Colombelli, W. Maineult, S. Barbieri, S. P. Khanna, E. H. Linfield, and A. G. Davies, *Opt. Express* **17**, 9491–9052 (2009).
7. G. Xu, R. Colombelli, R. Braive, G. Beaudoin, L. Le Gratiet, S. Bouchoule, A. Talneau, L. Ferlazzo, and I. Sagnes, *Opt. Express* **18**, 11979–11989 (2010).
8. G. Xu, V. Moreau, Y. Chassagneux, A. Bousseksou, R. Colombelli, G. Patriarche, G. Beaudoin, and I. Sagnes, *Appl. Phys. Lett.* **94**, 221101 (2009).
9. G. Xu, Y. Chassagneux, R. Colombelli, G. Beaudoin, and I. Sagnes, *Opt. Lett.* **35**, 859–861 (2010).
10. S. Hofling, J. Heinrich, H. Hofmann, M. Kamp, J. P. Reithmaier, A. Forchel, and J. Seufert, *Appl. Phys. Lett.* **89**, 191113 (2006).
11. L. A. Dunbar, V. Moreau, R. Ferrini, R. houdre, L. Sirigu, G. Scalari, M. Giovannini, N. Hoyler, and J. Faist, *Opt. Express* **13**, 8960–8968 (2005).
12. B. S. Williams, S. Kumar, H. Callebaut, Q. Hu, and J. L. Reno, *Appl. Phys. Lett.* **83**, 5142 (2003).
13. L. Sirigu, R. Terazzi, M. I. Amanti, M. Giovannini, J. Faist, L. A. Dunbar, and R. Houdre, *Opt. Express* **16**, 5206–5217 (2008).
14. A. Bousseksou, R. Colombelli, A. Babuty, Y. De Wilde, Y. Chassagneux, C. Sirtori, G. Patriarche, G. Beaudoin, and I. Sagnes, *Opt. Express* **17**, 9391–9400 (2009).
15. A. Farjadpour, D. Roundy, A. Rodriguez, M. Ibanescu, P. Bermel, J. D. Joannopoulos, S. G. Johnson, and G. Burr, *Opt. Lett.* **31**, 2972–2974 (2006).
16. A. F. Oskooi, D. Roundy, M. Ibanescu, P. Bermel, J. D. Joannopoulos, and S. G. Johnson, *Comput. Phys. Commun.* **181**, 687–702 (2010).

17. A. Taflove, *Computational Electrodynamics: The Finite-Difference Time-Domain Method*, Artech House, Norwood, MA (1995).
18. P. Viktorovitch, B. Ben Bakir, S. Boutami, J-L. Leclercq, X. Letartre, P. Rojo-Romeo, C. Seassal, M. Zussy, L. Di Cioccio, and J.-M. Fedeli, *Laser Photon. Rev.* **4**, 401–413 (2010).
19. A. Bousseksou, V. Moreau, R. Colombelli, C. Sirtori, G. Patriarche, O. Mauguin, L. Largeau, G. Beaudoin, and I. Sagnes, *Electron. Lett.* **44**, 807–808 (2008).
20. L. Magdenko, F. Gaucher, P. Lecoeur, M. Vanwolleghem, A. Aassime, and B. Dagens, *Microelect. Eng.* **86**, 2251–2254 (2009).
21. G. Vecchi, F. Raineri, I. Sagnes, A. Yacomotti, P. Monnier, T. J. Karle, K.-H. Lee, R. Braive, L. Le Gratiet, S. Guilet, G. Beaudoin, A. Talneau, S. Bouchoule, A. Levenson, and R. Raj, *Opt. Express* **15**, 7551–7556 (2008).
22. S. H. Kim, S. K. Kim, and Y. Hs. Lee, *Phys. Rev.* B **73**, 235117 (2006).
23. J. Vuckovic, M. Loncar, H. Mabuchi, and A. Scherer, *IEEE J. Quantum Electron.* **38**, 850–856 (2002).

Biographies and photographs of the authors not available.